Research Article | Vol. 9, No. 3 | 1 Mar 2018 | BIOMEDICAL OPTICS EXPRESS 952
Biomedical Optics EXPRESS

Phase-stable Doppler OCT at 19 MHz using a stretched-pulse mode-locked laser

SERHAT TOZBURUN,[1,2,3,*] CEDRIC BLATTER,[1,2] MEENA SIDDIQUI,[2,4] EELCO F. J. MEIJER,[1,5] AND BENJAMIN J. VAKOC[1,2,4]

[1]*Harvard Medical School, Boston, Massachusetts 02115, USA*
[2]*Wellman Center for Photomedicine, Massachusetts General Hospital, Boston, Massachusetts 02114, USA*
[3]*Izmir International Biomedicine and Genome Institute, Dokuz Eylul University, 35340 Balcova, Izmir, Turkey*
[4]*Harvard-MIT Division of Health Sciences and Technology, Cambridge, Massachusetts 02139, USA*
[5]*Edwin L. Steele Laboratory for Tumor Biology, Massachusetts General Hospital, Boston, Massachusetts 02114, USA*
**serhat.tozburun@deu.edu.tr*

Abstract: We present a swept-wavelength optical coherence tomography (OCT) system with a 19 MHz laser source and electronic phase-locking of the source, acquisition clock, and beam scanning mirrors. The laser is based on stretched-pulse active mode-locking using an electro-optic modulator. Beam scanning in the fast axis uses a resonant micro-electromechanical systems (MEMS) -based mirror at ~23.8 kHz. Acquisition is performed at 1.78 Gigasamples per second using an external fixed clock. Phase sensitive imaging without need for k-clocking, A-line triggers, or phase-calibration methods is demonstrated. The system was used to demonstrate inter-frame and inter-volume Doppler imaging in the mouse ear and brain at 4D acquisition rates of 1, 30, 60 and 100 volumes/sec (V-scans/s). Angiography based on inter-frame and inter-volume methods are presented. The platform offers extremely fast and phase-stable measurements that can be used in preclinical angiographic and Doppler investigations of perfusion dynamics.

OCIS codes: (140.3600) Lasers, tunable; (170.0110) Imaging systems; (170.4500) Optical coherence tomography.

References and links

1. D. Huang, E. A. Swanson, C. P. Lin, J. S. Schuman, W. G. Stinson, W. Chang, M. R. Hee, T. Flotte, K. Gregory, C. A. Puliafito, and J. G. Fujimoto, "Optical coherence tomography," Science **254**(5035), 1178–1181 (1991).
2. J. G. Fujimoto, M. E. Brezinski, G. J. Tearney, S. A. Boppart, B. Bouma, M. R. Hee, J. F. Southern, and E. A. Swanson, "Optical biopsy and imaging using optical coherence tomography," Nat. Med. **1**(9), 970–972 (1995).
3. A. F. Fercher, W. Drexler, C. K. Hitzenberger, and T. Lasser, "Optical coherence tomography – principles and applications," Rep. Prog. Phys. **66**(2), 239–303 (2003).
4. S. Yun, G. Tearney, J. de Boer, N. Iftimia, and B. Bouma, "High-speed optical frequency-domain imaging," Opt. Express **11**(22), 2953–2963 (2003).
5. R. Leitgeb, C. Hitzenberger, and A. Fercher, "Performance of Fourier domain vs. time domain optical coherence tomography," Opt. Express **11**(8), 889–894 (2003).
6. M. Choma, M. Sarunic, C. Yang, and J. Izatt, "Sensitivity advantage of swept source and Fourier domain optical coherence tomography," Opt. Express **11**(18), 2183–2189 (2003).
7. X. Wei, J. Xu, Y. Xu, L. Yu, J. Xu, B. Li, A. K. S. Lau, X. Wang, C. Zhang, K. K. Tsia, and K. K. Y. Wong, "Breathing laser as an inertia-free swept source for high-quality ultrafast optical bioimaging," Opt. Lett. **39**(23), 6593–6596 (2014).
8. J. Xu, X. Wei, L. Yu, C. Zhang, J. Xu, K. K. Y. Wong, and K. K. Tsia, "High-performance multi-megahertz optical coherence tomography based on amplified optical time-stretch," Biomed. Opt. Express **6**(4), 1340–1350 (2015).
9. T. Huo, C. Wang, X. Zhang, T. Chen, W. Liao, W. Zhang, S. Ai, J. C. Hsieh, and P. Xue, "Ultrahigh-speed optical coherence tomography utilizing all-optical 40 MHz swept-source," J. Biomed. Opt. **20**(3), 030503 (2015).
10. W. Wieser, B. R. Biedermann, T. Klein, C. M. Eigenwillig, and R. Huber, "Multi-megahertz OCT: High quality 3D imaging at 20 million A-scans and 4.5 GVoxels per second," Opt. Express **18**(14), 14685–14704 (2010).

#307234 https://doi.org/10.1364/BOE.9.000952
Journal © 2018 Received 18 Sep 2017; revised 13 Dec 2017; accepted 13 Dec 2017; published 2 Feb 2018

Biomedical Optics EXPRESS

11. T. Klein, W. Wieser, L. Reznicek, A. Neubauer, A. Kampik, and R. Huber, "Multi-MHz retinal OCT," Biomed. Opt. Express **4**(10), 1890–1908 (2013).
12. W. Wieser, W. Draxinger, T. Klein, S. Karpf, T. Pfeiffer, and R. Huber, "High definition live 3D-OCT in vivo: design and evaluation of a 4D OCT engine with 1 GVoxel/s," Biomed. Opt. Express **5**(9), 2963–2977 (2014).
13. D. Choi, H. Hiro-Oka, H. Furukawa, R. Yoshimura, M. Nakanishi, K. Shimizu, and K. Ohbayashi, "Fourier domain optical coherence tomography using optical demultiplexers imaging at 60,000,000 lines/s," Opt. Lett. **33**(12), 1318–1320 (2008).
14. D. H. Choi, H. Hiro-Oka, K. Shimizu, and K. Ohbayashi, "Spectral domain optical coherence tomography of multi-MHz A-scan rates at 1310 nm range and real-time 4D-display up to 41 volumes/second," Biomed. Opt. Express **3**(12), 3067–3086 (2012).
15. B. Potsaid, V. Jayaraman, J. G. Fujimoto, J. Jiang, P. J. S. Heim, and A. E. Cable, "MEMS tunable VCSEL light source for ultrahigh speed 60kHz – 1 MHz axial scan rate and long range centimeter class OCT imaging," Proc. SPIE **8213**, 82130M (2012).
16. B. White, M. Pierce, N. Nassif, B. Cense, B. Park, G. Tearney, B. Bouma, T. Chen, and J. de Boer, "In vivo dynamic human retinal blood flow imaging using ultra-high-speed spectral domain optical coherence tomography," Opt. Express **11**(25), 3490–3497 (2003).
17. R. A. Leitgeb, R. M. Werkmeister, C. Blatter, and L. Schmetterer, "Doppler optical coherence tomography," Prog. Retin. Eye Res. **41**, 26–43 (2014).
18. S. Makita, Y. Hong, M. Yamanari, T. Yatagai, and Y. Yasuno, "Optical coherence angiography," Opt. Express **14**(17), 7821–7840 (2006).
19. Z. Zhi, W. Qin, J. Wang, W. Wei, and R. K. Wang, "4D optical coherence tomography-based micro-angiography achieved by 1.6-MHz FDML swept source," Opt. Lett. **40**(8), 1779–1782 (2015).
20. H. Spahr, D. Hillmann, C. Hain, C. Pfäffle, H. Sudkamp, G. Franke, and G. Hüttmann, "Imaging pulse wave propagation in human retinal vessels using full-field swept-source optical coherence tomography," Opt. Lett. **40**(20), 4771–4774 (2015).
21. S. Wang, M. Singh, A. L. Lopez 3rd, C. Wu, R. Raghunathan, A. Schill, J. Li, K. V. Larin, and I. V. Larina, "Direct four-dimensional structural and functional imaging of cardiovascular dynamics in mouse embryos with 1.5 MHz optical coherence tomography," Opt. Lett. **40**(20), 4791–4794 (2015).
22. W. Wei, J. Xu, U. Baran, S. Song, W. Qin, X. Qi, and R. K. Wang, "Intervolume analysis to achieve four-dimensional optical microangiography for observation of dynamic blood flow," J. Biomed. Opt. **21**(3), 036005 (2016).
23. R. Huber, M. Wojtkowski, J. G. Fujimoto, J. Y. Jiang, and A. E. Cable, "Three-dimensional and C-mode OCT imaging with a compact, frequency swept laser source at 1300 nm," Opt. Express **13**(26), 10523–10538 (2005).
24. B. Vakoc, S. Yun, J. de Boer, G. Tearney, and B. Bouma, "Phase-resolved optical frequency domain imaging," Opt. Express **13**(14), 5483–5493 (2005).
25. B. Braaf, K. A. Vermeer, V. A. D. P. Sicam, E. van Zeeburg, J. C. van Meurs, and J. F. de Boer, "Phase-stabilized optical frequency domain imaging at 1-μm for the measurement of blood flow in the human choroid," Opt. Express **19**(21), 20886–20903 (2011).
26. S. Tozburun, M. Siddiqui, and B. J. Vakoc, "A rapid, dispersion-based wavelength-stepped and wavelength-swept laser for optical coherence tomography," Opt. Express **22**(3), 3414–3424 (2014).
27. E. Brown, L. L. Munn, D. Fukumura, and R. K. Jain, "In vivo imaging of tumors," Cold Spring Harbor Protoc. 2010(7), pdb.prot5452, (2010).
28. B. H. Park, M. C. Pierce, B. Cense.SH. Yun, M. Mujat, G. J. Tearney, B. E. Bouma, and J. F. de Boer, "Real-time fiber-based multi-functional spectral-domain optical coherence tomography at 1.3 μm," Opt. Express **13**(11), 3931–3944 (2005).
29. J. Fingler, D. Schwartz, C. Yang, and S. E. Fraser, "Mobility and transverse flow visualization using phase variance contrast with spectral domain optical coherence tomography," Opt. Express **15**(20), 12636–12653 (2007).
30. D. M. Schwartz, J. Fingler, D. Y. Kim, R. J. Zawadzki, L. S. Morse, S. S. Park, S. E. Fraser, and J. S. Werner, "Phase-Variance Optical Coherence Tomography: A Technique for Noninvasive Angiography," Ophthalmology **121**(1), 180–187 (2014).
31. R. E. Meyer and R. E. Fish, "WIII. Anesthetic Combinations" in Chap. 2. in Anesthesia and Analgesia in Laboratory Animals, R. Fish, P. J. Danneman, M. Brown, and A. Karas ed. (Academic Press, 1997).
32. R. K. Wang, Z. Ma, and S. J. Kirkpatrick, "Tissue Doppler optical coherence elastography for real time strain rate and strain mapping of soft tissue," Appl. Phys. Lett. **89**(14), 144103 (2006).

1. Introduction

Optical coherence tomography (OCT) is a noninvasive imaging modality [1–3] providing high-resolution, three-dimensional imaging of biological tissue. Fourier-domain OCT has significantly improved the capability of this modality enabling high speed and sensitive imaging [4–6]. Laser technologies based on dispersive time stretching [7–9] and Fourier-domain mode-locking (FDML) have enabled megahertz imaging speeds [10–12]. Spectral-domain OCT using a fast spectrometer has achieved ultrafast A-scan rates [13,14]. VCSEL-

Biomedical Optics EXPRESS

based laser technology has provided a sweep rate of 1 MHz [15]. These imaging speeds can be leveraged to improve and accelerate blood flow imaging [16] and angiography [17,18]. Examples include 4D OCT angiography of micro-vascular dynamics [19–22].

In this work, we demonstrate a Doppler and angiographic OCT system using a 19 MHz swept wavelength source integrated with a MEMS-based ~23.8 kHz fast-axis scanner. The rapid acquisition of A-lines allows phase-based angiographic analyses between frames and between volumes with much shorter time separations. Importantly, the source, digitizer, and MEMS scanner can be electronically phase-locked to provide an intrinsically phase stable imaging system. This greatly simplifies Doppler measurements, and eliminates the need for A-scan triggers [23] or post-processing phase calibration algorithms [24,25]. The system is integrated with a 1.78 Gigasamples (GS) per second acquisition card supporting continuous acquisition of a single channel to computer random access memory, or RAM, for ~10.7 s. The speed and phase-stability of the laser and MEMS scanner platform can be leveraged to enable to accelerate and simplify OCT-based angiography and volumetric blood flow quantification.

2. Experimental system setup

2.1 Stretched-pulse mode-locked (SPML) laser source

Figure 1 shows a schematic of the OCT system used in this work. The operating principle of SPML laser source (Fig. 1(A)) was described in detail in Ref [26]. Briefly, the laser comprised a unidirectional ring cavity with intracavity matched positive and negative dispersive fibers. A 19.929-km SMF-28e + fiber spool with a single-pass optical loss of 3.52 dB was used to generate positive dispersion. The spool was used with a Faraday rotator mirror in double-pass configuration to generate a total dispersion of + 657 ps/nm at the center wavelength of 1550 nm. Negative dispersion was generated by a single-pass dispersion-compensating fiber (5.26 km in length, 2.96 dB optical loss) designed to be dispersion slope matched to the SMF-28e + fiber. The group delay of the combined dispersive fibers was measured to be 237.4 μs across the lasing bandwidth. Variations in group delay were on the order of ± 0.20 ns. Two semiconductor optical amplifiers (SOAs) were used as gain elements in the laser to overcome high losses due to the long dispersive fiber lengths (BOA1004S, Thorlabs, NJ, USA). A lithium-niobate intensity modulator (MXER-LN, Photline Technologies, France), having 4.3 dB loss at maximum transmission was driven with short electrical pulses by a bit pattern generator (PAT 3000, Sympuls, Germany) providing approximately 0.32 ns full-width at half-maximum optical pulse profiles. These pulses were stretched, amplified, and compressed within the ring cavity, and the modulator pulsing was synchronized to a harmonic of the cavity round trip time. Laser output was provided from the cavity by a 20% tap coupler. Output light was amplified outside the cavity by a third SOA. The output power was 32 mW. The laser source provided a sweep range of approximately 74 nm centered at around 1550 nm at a sweep rate of 19 MHz. The laser source did not sweep linearly with wavenumber, and required chirp correction in post-processing. Windowing lead to an effective FWHM bandwidth of approximately 37 nm, yielding an axial resolution of 21 microns in tissue.

Biomedical Optics EXPRESS

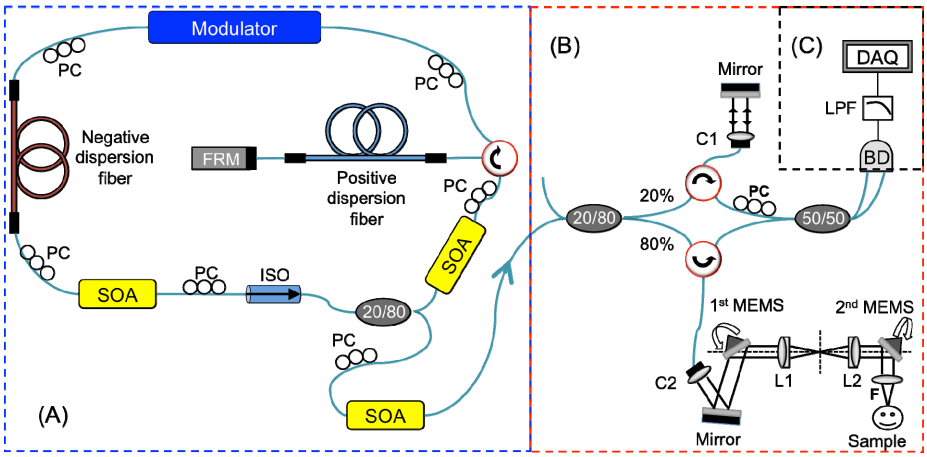

Fig. 1. A schematic of the phase stable OCT system. (A) 19-MHz stretched-pulse mode-locked (SPML) laser source. (B) Interferometer and scanner. (C) Data acquisition system. PC: polarization controller; SOA: semiconductor optical amplifier; ISO: isolator; FRM: Faraday rotating mirror; C1: collimator (f = 11 mm); C2: collimator (f = 3.9 mm); L1: lens (f = 50 mm); L2: lens (f = 50 mm); f: focusing lens (f = 10 mm). LPF: low pass filter (780 MHz); BD: balanced detector (1.6 GHz); DAQ: data acquisition card (~1.78 GS/s); MEMS1: slow-axis MEMS-based scanner (at rates of 1, 30, 60 and 100 volumes per second); MEMS2: fast-axis MEMS-based scanner (at the B-scan rate of 23.786 kHz).

2.2 Interferometer and microscope

The fiber based Mach-Zehnder interferometer is shown in Fig. 1(B). Laser light was coupled into the interferometer through the 20/80 coupler, where it was split into a sample arm (80%) and a reference arm (20%). The reference beam travelling through a circulator was aimed at a mirror with a fixed distance and the back-reflected light was coupled back into the circulator. In the sample arm, there was an imaging lens (F) and a 2D microscope comprising two separate MEMS scanners (S12236-08P, Hamamatsu, Japan) with an intermediate optical relay. Collimated light with a ~1 mm beam diameter was launched to the MEMS scanners, which have 1 mm mirror size. A 10 mm focal length imaging lens (AC080-010-C, Thorlabs, USA) was used after the second scanner providing a 4 mm (fast axis) by 2 mm (slow axis) scan area. The back-scattered light was then collected back into the fiber circulator and the light was recombined at a 50/50 coupler. The lateral resolution was calculated to be 18 μm at the sample. The imaging depth range was limited to >490 μm in tissue due to RF acquisition bandwidth limitations. The power of the scanning light at the sample was 10 mW.

2.3 Scanning protocol

An area of 8 mm^2 (4 mm in the fast axis by 2 mm in the slow axis) was imaged. Both MEMS mirrors were driven with sinusoidal waveforms generated by two separate function generators. The MEMS scanner in the fast axis (1st MEMS scanner) at a resonance frequency of ~23.8 kHz provided a scanning range of ± 16.0 degrees (optical angle) with a driving voltage level of 6.0 Vpp. The scanning range of the 2nd MEMS scanner in the slow axis was ± 8.0 degrees in optical angle with a voltage of 4.0 Vpp at a frequency of 60 Hz. Each volumetric data set was acquired over the entire cycle of the sinusoidal waveform in both axes. However, only the forward scan was used to generate image data. Because of the sinusoidal motion of the MEMS scanners, resampling was applied in both axes.

2.4 Data-acquisition and phase-locked electronics

Fringe signals from the interferometer were detected with a 1.6-GHz balanced detector (PDB480C-AC, Thorlabs, NJ, USA) and filtered using a low-pass filter (BLP750 + , Mini-

Biomedical Optics EXPRESS

circuits, NY, USA) with a cutoff frequency of 780 MHz to remove high frequency components (Fig. 1(C)). Signals were digitized with 12 bit resolution at sampling frequency of ~1.78 GS/s (ATS9360, AlazarTech, Canada). Fringe signals were captured continuously (i.e., without A-line triggers) resulting in a 3.56 GS/s data-stream (1.78 GS/s x 2 bytes per sample). Signals were acquired for up to 10.7 seconds. A radio frequency signal generator (RF signal generator) clocked the acquisition. LabVIEW was used to provide real-time display for sample alignment. Fringe capture was performed using the AlazarTech digital storage oscilloscope (DSO) application.

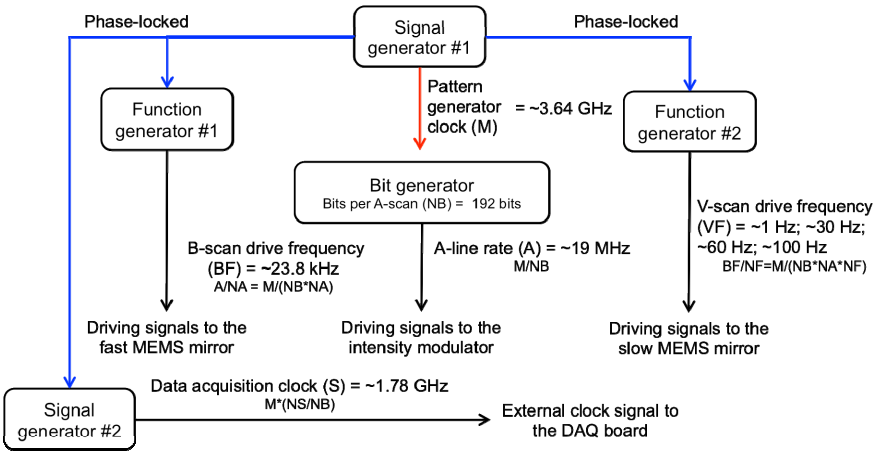

Fig. 2. A schematic of the electronic clocks and synchronization scheme.

The phase-locking configuration of the laser, the acquisition system, and MEMS drivers is shown in Fig. 2. All components were locked to a master clock, and drive frequencies were set as integer multiples of each other to produce intrinsically phase stable fringes/A-scans. Table 1 summarizes the frequency values and the relations between them. The bit generator was externally clocked at ~3.64 GHz by a RF signal generator (SG384, Stanford Research System, CA, USA). The second RF signal generator provided a clock signal to the data acquisition (DAQ) board at a sampling rate of ~1.78 GHz. A total of 94 samples were acquired per A-scan at the 19 MHz sweep rate. Phase-locked function generators drove two separate MEMS scanners providing 798 A-scans at ~23.8 kHz in the fast axis (1st MEMS); and 792 B-scans at 30 V-scans/s, 396 B-scans at 60 V-scan/s, and 237 B-scans at 100 V-scans/s in the slow axis (2nd MEMS), respectively.

Table 1. The relations between all electronic components phase-locked to a master clock.

Parameter	Value	Relationship
Pattern generator clock (M)	3.644 412 400 GHz	-
Bits per A-scan (NB)	192 bits	-
A-line rate (A)	18.981314583333 MHz	M/NB
Samples per A-line (NS)	94 samples	-
Data acquisition clock (S)	1.784243570833330 GHz	M*(NS/NB)
A-line per B-scan (NA)	798 A-lines	-
B-scan drive frequency (BF)	23.786108500 kHz	A/NA = M/(NB*NA)
Frames per Volume (NF)	23798; 792; 396; 237	-
V-scan drive frequency (VF)	1.000005 Hz; 30.032965 Hz; 60.065931 Hz; 100.363327 Hz	BF/NF = M/(NB*NA*NF)

2.5 Post-processing

Post data processing was performed in Matlab (Mathworks, MA, USA). The data processing steps were the following. (A) Conventional OCT image processing was applied to obtain the complex depth encoded data, including background subtraction for reducing the direct current

Biomedical Optics EXPRESS

(DC) terms and the fixed-pattern noises, resampling by spline interpolation from lambda to k-space, windowing by a Hanning-window for spectral shaping of the spectrum, and a zero-padded fast Fourier transformation on each A-scan to increase the axial-data array size to 140. (B) Only half of the imaging depth was useful due to mirror image artifacts caused by complex conjugate ambiguity. In addition, only the forward scanning was used in both scan directions. Therefore, final 4D complex OCT data sets of 70 by 399 by 11893 by 1 for 1 V-scan/s, 70 by 399 by 396 by 320 for 30 V-scans/s, 70 by 399 by 198 by 640 for 60 V-scans/s and 70 by 399 by 118 by 1070 for 100 V-scans/s were generated, respectively, as detailed in Table 2. (C) The volumetric data sets were linearly rescaled by spline interpolation to remove the sinusoidal driving waveform in the transverse (fast) and in the lateral (slow) axes. (D) Each pixel of both logged amplitude and phase information was then stored separately in 8-bit scale for further process. (E) The logarithmic intensity scaling for structural OCT image construction was performed. (F) High-pass filtering was applied to the phase signal to remove slow bulk motion signals.

Table 2. Specifications of V-scans and data sets.

Volume rate (V-scans/s)	Number of V-scans	Raw V-scan size (voxels)	Processed V-scan size (voxels)	Time of acquisition (s)
1	1	94x798x23786	70x399x11893	1.00
30	320	94x798x792	70x399x396	10.67
60	640	94x798x396	70x399x198	10.67
100	1070	94x798x237	70x399x119	10.70

2.6 Animal preparation

All *in vivo* imaging studies were performed under an animal protocol approved and in compliance with Institute of Animal care and Use Committee (IACUC) policies governing the care and use of animals at Massachusetts General Hospital (Boston, MA). A total of 3 mice (26 to 32 g) were anesthetized by subcutaneous injection with ketamine (90 mg/kg)-xylazine (9 mg/kg) solution. Two nude female mice (12 weeks old) were used for mouse ear imaging. The dorsal face of the right ear was carefully placed in place after a small water drop was applied to reduce the mismatch of the refractive index between the air and the ear. The mouse brain was imaged through a cranial window. The window was implanted on the cortex area of an 8 weeks old female BALB/c mouse as described in detail in Ref [27]. During brain imaging, the mouse was placed in prone position and held stable using a custom build stereotactic apparatus to minimize motion artifacts.

3. Results and discussion

In this section, we quantify the phase-stability of the OCT system. We present a set of *in vivo* imaging experiments in mice to demonstrate the capability of the system. These experiments include inter-frame Doppler OCT, inter-volume phase variance OCT angiography, and inter-volume Doppler OCT.

3.1 OCT system phase stability

Here, we demonstrate that the OCT system provides high degree of phase coherence between successive V-scans over several seconds and without requiring individual A-line triggers or implementation of post-processing phase calibration algorithms. This is enabled by the inherent stability of the swept-wavelength source that is phase-locked to the data acquisition electronics and MEMS-based scanners. Two studies have been performed in this section. In the first study, OCT A-scans of a rubber phantom were generated at a single location for a period of ~10 s. Figure 3(A) shows 5 fringe signals. The measured phase of the peak signal for each A-line is plotted in Fig. 3(B). The phase noise was ± 19 mrad (standard deviation), matching the predicted phase noise from the 31 dB signal [28].

Biomedical Optics EXPRESS

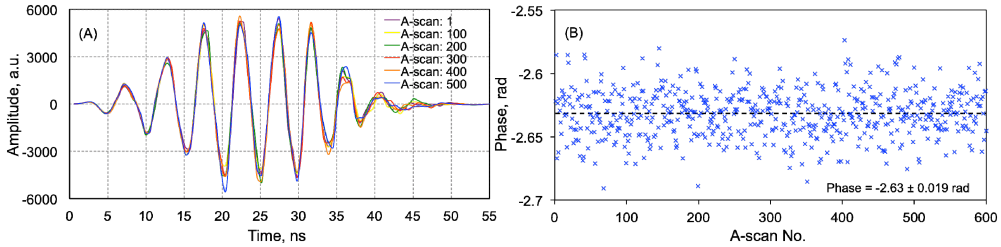

Fig. 3. (A) Representative fringe signals of selected A-scans. The corresponding phase values as a function of consecutive A-scans at the single depth that has the peak signal estimated from OCT amplitude information are shown in panel B. The measured phase noise at peak signal (SNR = 31 dB) was ± 0.019 rad.

Because of the high phase stability, acquired complex tomographic signals can be added directly in post-processing to improve SNR in static tissues to reveal phase washout driven signal fading in flowing blood. To demonstrate this, volumetric acquisitions of a mouse ear were acquired in the second study. A structural image from a single volume acquisition is shown in cross-section and *en face* at 100 V-scans/s in Fig. 4(A), 4(B). Multiple volumes were coherently averaged (i.e., averaging the complex A-scan signals of each voxel) without applying phase calibration or correction. The resulting cross-sectional and *en face* structure images for 9 and 81 averaged volumes are presented in Fig. 4(C)-4(F). Note the fading of the intravascular signal due to effects of phase washout, while the static tissue signal remains and increases in SNR relative to the first volume. The coherent averaging maintains the relative intensity of the signal at the static tissue and reduces the relative intensity at the microvasculature tissue as a function of number of image volumes (N), as shown in Fig. 4(G)-4(I).

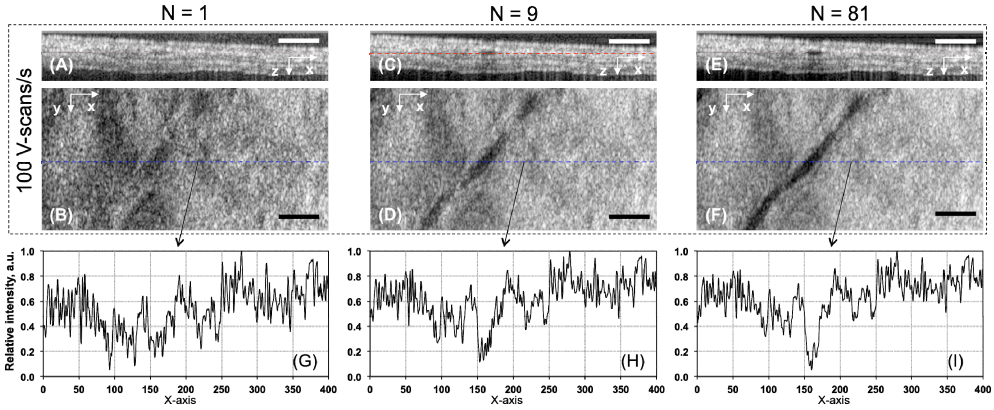

Fig. 4. Inter-volume coherent averaging of 4D images acquired in an *in vivo* mouse ear. Cross-sectional and *en face* OCT images of the tissue for N coherently averaged volumes: N = 1 (panel A,B), N = 9 (panel C,D), and N = 81 (panel E,F). Dash-dot red lines show the depth of *en face* presentations and dash-dot blue lines show the location of cross-sectional images. Panels G-I show relative intensity along the x-axis. Scale bar = 500 µm.

3.2 Inter-frame Doppler OCT

In Fig. 5, we illustrate an inter-frame Doppler OCT analysis capability of the system at the high frame rate of 23.786 kHz. Because of the high frame rate, these inter-frame Doppler measurements largely avoid phase wrapping artifacts. In this study, the scan rate of slow axis was set to be 1 V-scan/s to generate oversampling in the slow-axis dimension. The frames were first grouped in sets of 10. These sets of 10 frames were coherently averaged to improve SNR. Next, the phase difference between coherently averaged frames was calculated. The

Biomedical Optics EXPRESS

time difference for this phase comparison was 10 frames (23.786 kHz/10 ≈2.38 kHz). Color encoding of the Doppler information demonstrated in Fig. 5 clearly distinguishes the vessels at a single depth of 180 μm within the tissue. The Doppler signal changes sign along a single vessel due to the its varying Doppler angle. It is because the imaged vessels are close to perpendicular to the beam (Doppler angle near 90°). Small physical changes that occur due to respiration and heartbeat shift the angle above and below Doppler angle, resulting in changes in the sign of the phase change.

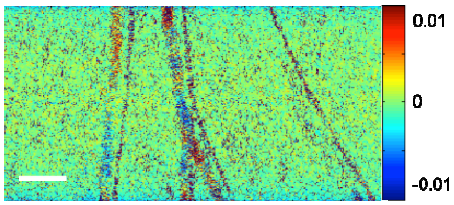

Fig. 5. *En face* inter-frame Doppler OCT image at a depth of 180 μm in the mouse ear. Color bar shows the phase difference ranging from –0.01 to 0.01 rad. Scale bar = 500 μm.

3.3 Inter-volume phase variance angiography

We next explored inter-volume phase variance angiography. In phase variance based angiography, the source of contrast is the higher variance of phase differences in the areas of flow relative to areas of static tissue [29]. Due to the effective suppression of phase difference variance in static tissue over time, the method provides high contrast between the vessel networks and the surrounding static tissue that allows easier identification of vessels [30]. In this section, we measured the variance of the phase over consecutively acquired V-scans during 4D scanning in a mouse ear. First, we calculated the phase differences between consecutive V-scans to provide phase contrast information over time. Then, the phase variance signals were extracted by using phase difference data relative to the adjacent volume (i.e., $\Delta\varphi(x,y,z,t_{i+1}) - \Delta\varphi(x,y,z,t_i)$).

The volume rate was set to 30 V-scans/s, yielding a total number of 320 V-scans for the time duration of ~10.7 s. Figure 6 shows a projection view of the microvasculature across depths from 50 μm to 470 μm (Visualization 1). Regions of interest are enlarged to illustrate the fast morphological changes of structure in short period of time (see in panels D, E, and F in Fig. 6). Rapid 4D angiography allows evaluation of pulsatile changes in vascular morphology. For this purpose, we resampled the selected area of the projected image (area under dash-dot yellow boxes) along time axis. Figures 6(G), 6(H) plot the average angiography signal over time and reveal, morphological changes due to pulsation. The pulse rate was approximately ~160 bpm, in agreement with that expected from a BALB/c mouse under anesthesia [31].

Biomedical Optics EXPRESS

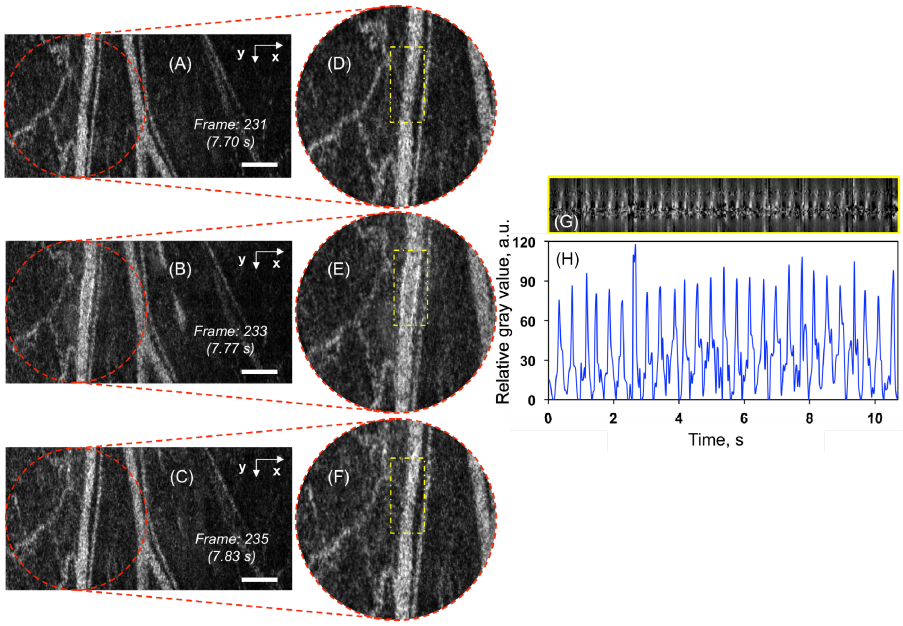

Fig. 6. Angiography performed across volumes using a method of inter-volume phase variance angiography. The frames in panels A (7.70 s), B (7.77 s), and C (7.83 s) were obtained from Visualization 1 at 30 fps. Enlarged views of the circle area from the panels highlight the morphology of microvascular structure and also change in morphology in time (panels D, E, and F). Panel G shows the changes of intensity along the time and panel H shows the corresponding relative grey values as a function of time after resampling the selected data. The total number of beats were measured to be ~160 bpm. Dash-dot yellow boxes indicate locations of the selected data. Scale bar = 500 µm.

3.4 Inter-volume Doppler OCT

Another attractive feature of the presented swept-source OCT system is that inter-volume Doppler OCT imaging can be obtained at video rate. Here, we described how the phase signal of V-scans relative to a reference time (i.e., $\varphi(t)$ - $\varphi(t_{ref})$) provided volumetric Doppler information over time to show a potential of monitoring pulsatile dynamics including pulse-driven tissue compression. In the experiment, imaging sessions were performed through a cranial window. As detailed in subsection 2.3, the brain surface was scanned over 4 mm in x-direction (fast-axis) and 2 mm in y-direction (slow-axis). The acquisition time was ~10.7 s at a volume rate of 60 V-scans/s. Each volume consisted of 198 B-scans and each B-scan had a size of 70 by 399 pixels (see Table 2). Then, voxel phase information sets of 640 V-scans were used to generate 4D (x,y,z,t) inter-volume Doppler OCT by processing the phase difference along the successive V-scans relative to a reference V-scan.

We employed the method of inter-volume phase variance angiography as described in subsection 3.3 to visualize vasculature structure within the scanning area of the mouse brain. Figure 7(A) shows a representative *en face* projection view at the depths from 40 µm to 460 µm. Axial displacement images were calculated from the phase information across as described in Ref [32]. for inter B-scan Doppler. The axial displacements for each volume (relative to the reference volume, 640th V-scan) were combined into a video (Visualization 2). Each frame in the video was the average displacement from 40 µm to 460 µm. Panels B, C and D in Fig. 7 present specific frames from this video. Displacements in the tissues surrounding the vessels are clearly visualized.

The displacement data within the dash-line yellow boxes was analyzed to identify the pulsatile frequency (102 bpm). The phase data were then Fourier transformed, and the amplitude and phase at 1.7 Hz (102 bmp) extracted. An *en face* projection of this

Biomedical Optics EXPRESS

amplitude/phase averaged across a depth range from 40 µm to 460 µm is presented in Fig. 7(E). This is an example of using the rapid 4D Doppler imaging system to analyze pulse-driven mechanical compression of tissues.

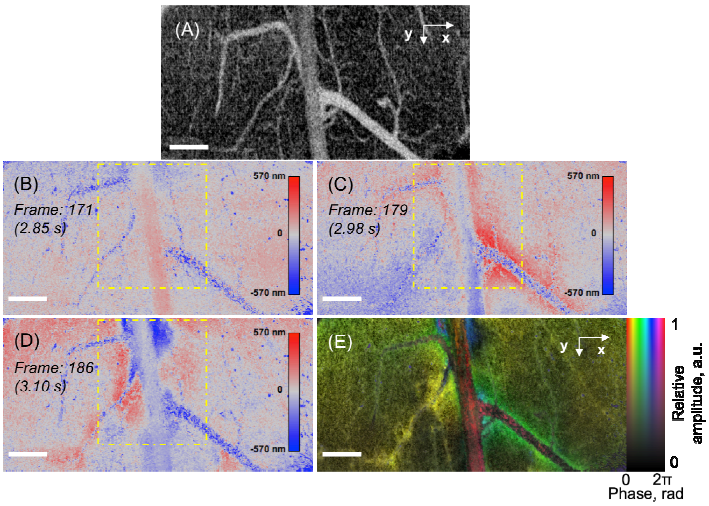

Fig. 7. (A) Projected image of inter-volume phase variance OCT angiography in an *in vivo* mouse brain to visualize the vasculature structure in the scanning area at the depths from 40 µm to 460 µm. Panels B, C, and D present *en face* Doppler OCT images extracted from Visualization 2 at time points of 2.85 s, 2.98 s, and 3.10 s. The calculated axial displacement in red-blue color map scaling from −570 nm to 570 nm demonstrates Doppler shift information within the adjacent tissue during imaging. (E) A projected image of the amplitude and phase of the Doppler signal at 102 bpm. Scale bar = 500 µm.

4. Conclusion

In this work, we have demonstrated a 19 MHz swept-source OCT system capable of providing rapid, phase-stable measurements for Doppler analysis across frames and volumes. We demonstrated inter-frame Doppler OCT angiography at a 23.8 kHz frame rate. To show rapid 4D angiographic imaging, inter-volume Doppler and inter-volume phase variance methods were employed. The results indicated that this rapid OCT system allowed observing the morphologic changes in microvasculature of pulsatile blood flow dynamics. We have also highlighted the ability of the system to provide the measurement of axial displacements in the tissues surrounding vessels in response to pulsation. The speed and phase-stability of this system can be leveraged to provide new methods in OCT-based angiography and both phase-sensitive and phase-insensitive extraction of blood flow velocity and pulsatile blood flow dynamics.

Funding

Center for Biomedical OCT Research and Translation (P41EB015903) awarded by the National Center for Research Resources; National Institute of Biomedical Imaging and Bioengineering of the National Institutes of Health (R01CA163528 and DOD FA9550-11-1-0331); Swiss National Science Foundation (P2SKP2_158640).

Acknowledgments

Cedric Blatter was supported by a Swiss National Science Foundation early post-doctoral mobility fellowship (P2SKP2_158640).

Disclosures

The authors declare that there are no conflicts of interest related to this article.